Article

Graphene oxide-polydopamine membranes with controlled interlayer spacing

https://doi.org/10.1038/s41586-026-10765-4

Received: 10 April 2025

Accepted: 4 June 2026

Published online: 15 July 2026

Open access

Check for updates

Youhua Lu[1,11], Laiyang Wei[2,11], Zi-an Xie[1,11], Xuefei Wu[3,4,11], Han Xue[1]✉, Huimei Su[1], Jie Liu[3], Mengfei Jing[1], Junjie Chen[5], Guosheng Shi[5], Zhenhuang Su[6], Fenggang Bian[6], Zhi-Kang Xu[7], Chongqin Zhu[2]✉, Wei-Hai Fang[2], Xiao Cheng Zeng[8,9]✉ & Jianjun Wang[1,10]✉

Stacked graphene oxide membranes (GOMs) show exceptional capabilities for high-throughput sieving of water, ions and molecules, offering transformative potential in environmental and energy sectors[1–5]. However, achieving GOMs with subnanometre interlayer spacing and subangstrom tunability while maintaining their structural robustness for rapid and selective ion transport remains a big challenge[6–8]. Here we present polydopamine-pillared composite GOMs with tunable and stable interlayer spacing, featuring controllable interlayer spacing down to 5.9 Å in the dry state, and capable of sieving hydrated rubidium (Rb^+) and potassium (K^+) ions differing in size by less than 0.1 Å in aqueous environments, achieving an Rb^+/K^+ separation factor of 5,320. These composite GOMs were fabricated by using the dopamine assembly and reaction timescale separation method. Specifically, the GOM fabrication capitalizes on the fact that nanoconfined water has a lower freezing temperature than that of bulk water, such that the interlayer spacing is regulated by the rapid assembly of dopamines into nanopillars, driven by nanoconfined liquid water while the surrounding is in bulk ice. The assembly process can be halted anytime by further lowering the temperature to tune and fix the interlayer spacing. Thereafter, the GOM is rigidified through the slower chemical reactions, including polymerization of dopamine molecules and covalent bonding at specific oxygen-containing sites on the graphene oxide surface while retaining ample graphene subnanochannels for high-flux transportation. The GOMs deliver continuous freshwater production for 30 days at a water permeance of 67.9 l m^{-2} h^{-1} bar^{-1}, 1–2 orders of magnitude higher than conventional membranes[9].

Stacked graphene oxide membranes (GOMs), with their unique structures of carbon-based channels that allow highly efficient water transport and tunable subnanometre interlayer spacing[4,7,8], have emerged as nature-inspired materials for applications in nanofluidics and environmental sciences[7,8,10,11]. To emulate biological subnanopores and to achieve both high water throughput and selective ion sieving[12], it is crucial to maintain the structural stability and accuracy of the interlayer spacing of GOMs in aqueous environments[13,14]. Over the past decades, various methods have been explored to modulate and stabilize the interlayer spacing of GOMs[7,8,13,15]. Notably, covalently crosslinking the oxygen-containing functional groups on adjacent graphene oxide (GO) sheets with intercalated molecules or nanomaterials has effectively stabilized the interlayer spacing of stacked GOM structures, which nevertheless results in a single fixed spacing determined by the geometry of the specific crosslinker[6,16]. Furthermore, the π–cation interaction between metal ions and GO sheets has been used to tune the interlayer spacing of GOMs by altering the types of cation, but the distinct sizes of the metal ions lead to discrete spacing values[7]. Therefore, achieving continuous and robust spacing regulation of GOMs at the subangstrom scale for universal ion sieving remains a big challenge, which has hindered the development of highly efficient water–salt separation and accurate cation-ion-sieving systems[1,7].

Here we report a dopamine (DA) molecular assembly and reaction timescale separation strategy, in which the assembly process (occurring within minutes) yields DA nanopillars for regulating the interlayer spacing while the reaction process (occurring over hours) yields the polydopamine (PDA) nanopillars bonded with GOs for stabilizing the interlayer spacing of the composite GOMs. Specifically, a key step in the GOM fabrication is controlling the experimental temperature to freeze bulk water into ice while maintaining the nanoconfined water

[1]Technical Institute of Physics and Chemistry, Chinese Academy of Sciences, Beijing, China. [2]College of Chemistry, Key Laboratory of Theoretical and Computational Photochemistry of Ministry of Education, Beijing Normal University, Beijing, China. [3]Institute of Chemistry, Chinese Academy of Sciences, Beijing, China. [4]Materials Sciences Division, Lawrence Berkeley National Laboratory, Berkeley, CA, USA. [5]Shanghai Key Laboratory of Atomic Control and Application of Inorganic 2D Supermaterials, State Key Laboratory of Materials for Advanced Nuclear Energy, Shanghai Applied Radiation Institute, Shanghai University, Shanghai, China. [6]Shanghai Synchrotron Radiation Facility, Shanghai Advanced Research Institute, Chinese Academy of Sciences, Shanghai, China. [7]Department of Polymer Science and Engineering, Zhejiang University, Hangzhou, China. [8]Department of Materials Science and Engineering, City University of Hong Kong, Kowloon, Hong Kong. [9]Hong Kong Institute for Clean Energy, City University of Hong Kong, Kowloon, Hong Kong. [10]Suzhou Institute for Advanced Research, University of Science and Technology of China, Suzhou, China. [11]These authors contributed equally: Youhua Lu, Laiyang Wei, Zi-an Xie, Xuefei Wu. ✉e-mail: xuehan@mail.ipc.ac.cn; cqzhu@bnu.edu.cn; xzeng26@cityu.edu.hk; wangjianjun@mail.ipc.ac.cn

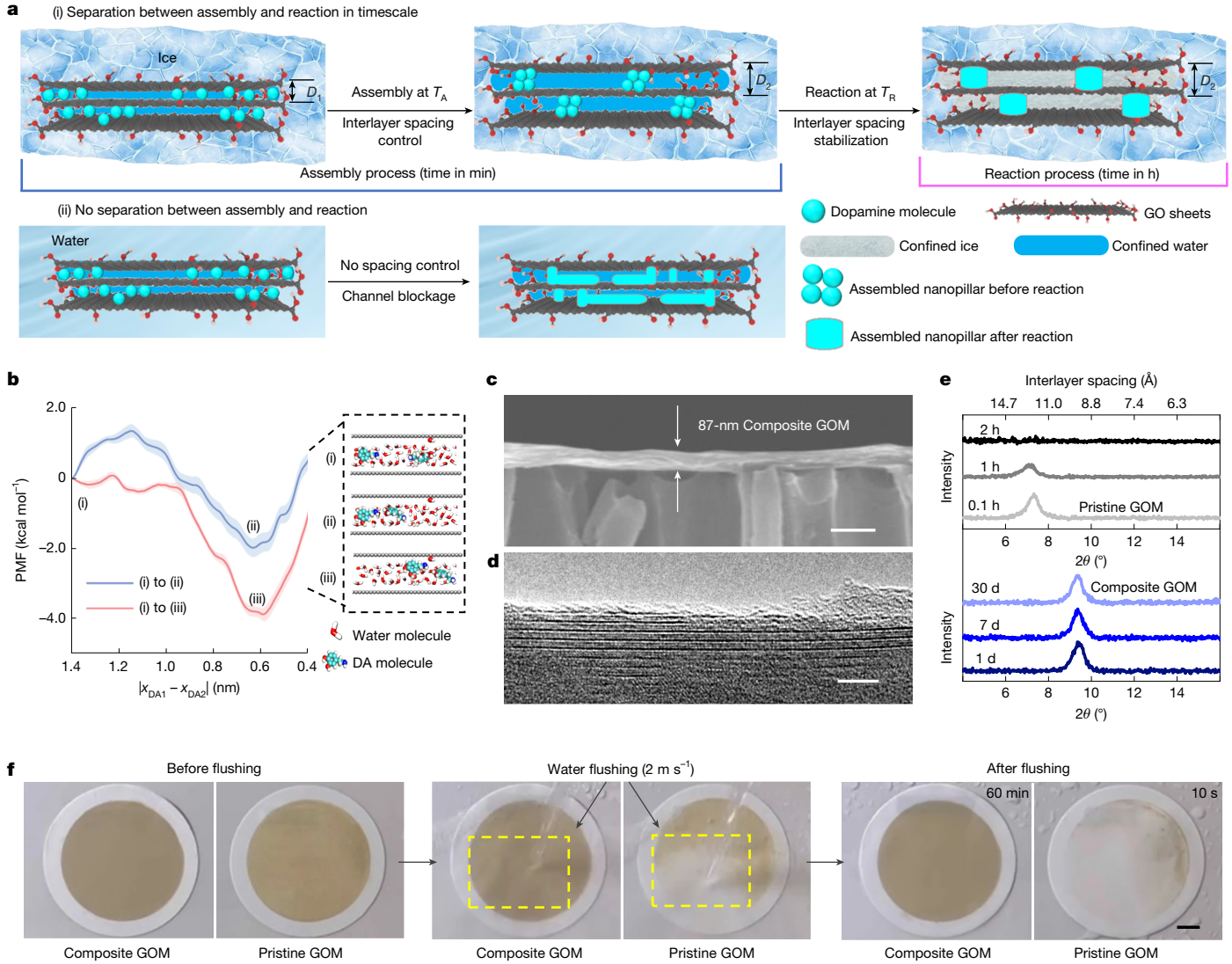

Fig. 1 | Timescale separated assembly and reaction strategy for preparing composite GOMs and characterizations of the GOMs. a, Scheme of modulating and stabilizing the composite-GOM interlayer spacing (D_1 to D_2). The DA molecules are marked as light-blue balls. The light-blue cylinders represent the postreaction PDA nanopillars. The grey-black sheet-like images represent GO sheets. The blue strips represent confined water. The grey cracked strips represent confined ice. The blue blocks with fragmented cracks represent bulk ice, and the blue blocks without fragmented cracks represent bulk water. **b**, The relationship between the computed potential of mean force and the collective variable (the distance between two DA molecules, $|x_{DA1} - x_{DA2}|$). In (i), one DA is near an oxygen-containing group. From (i) to (ii) (blue line), the DA near the oxygen-containing group is pulled towards the other DA. From (i) to (iii) (red line), the distant DA is pulled towards the oxygen-containing group. The right panel provides the schematic representation of configurations (i), (ii) and (iii). **c**,**d**, Cross-sectional scanning electron microscopy (**c**) and TEM (**d**) images of selected area of the composite GOM. **e**, Comparison of anti-swelling properties of pristine GOMs (top panel) and composite GOMs (bottom panel) by XRD patterns. Time of immersion with water: composite GOMs: 1 d (units of days) (dark blue), 7 d (blue), 30 d (light blue); pristine GOMs: 0.1 h (units of hours) (light grey), 1 h (grey), 2 h (black). **f**, Photographs of pristine GOM and composite GOMs under water flushing at 2 m s^{-1}. PMF, potential of mean force. Scale bars, 200 nm (**c**), 5 nm (**d**), 10 mm (**f**).

between GO sheets in a liquid state as illustrated in Fig. 1a. The retained mobility of nanoconfined liquid water facilitates the assembly of DA molecules within the interlayer space, where the assemblies act as DA nanopillars to finely adjust the interlayer spacing (D). After impregnating the interlayer space of the pristine GOM with the DA molecules (details in Supplementary Fig. 1), the processed GOM containing the DA molecules is then kept at a controlled temperature for assembly, T_A (for example, −10 °C) (left-top panel of Fig. 1a). During this assembly process, bulk ice forms around the GOM to prevent swelling (details in Supplementary Fig. 2), while the nanoconfined water between GO sheets remains mobile as the melting temperature of the bulk ice is higher than that of the nanoconfined ice. The diffusion of nanoconfined liquid water promotes the assembly of DA molecules into DA nanopillars of a targeted height to achieve the desired interlayer spacing within minutes, thereby tuning the GOM interlayer spacing (centre-top panel of Fig. 1a). Afterwards, the system is rapidly cooled to a lower reaction temperature T_R (below −30 °C) to convert the nanoconfined liquid water into nano-ice (detailed in Extended Data Fig. 1 and Supplementary Figs. 3 and 4), halting water molecule diffusion and the assembly process. Meanwhile, the polymerization of the DA molecules and covalent bonding between the polymerized DA and functional groups on GO surfaces continue in the nanoconfined-ice environment over hours, fixing the interlayer spacing (right-top panel of Fig. 1a). Note that without temporal separation of the DA assembly and DA polymerization reactions—whether relying solely on reactions or allowing assembly and reaction to occur simultaneously—the interlayer spacing would be difficult to control or tune. In either case, the reacted DA molecules would be more likely

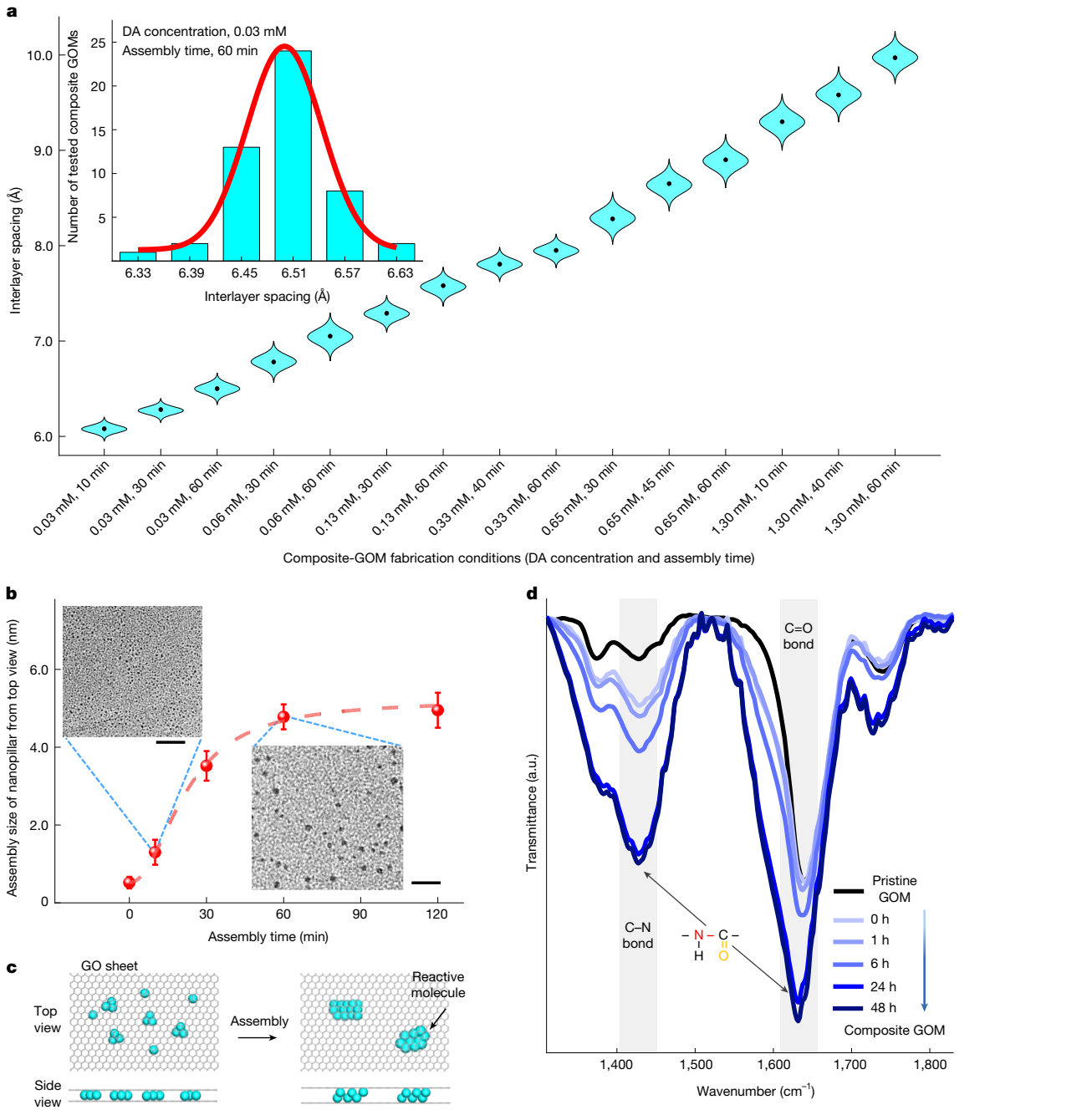

Fig. 2 | Regulating and stabilizing the interlayer spacing of the GOMs. **a**, XRD-derived interlayer spacing can be continuously tuned by varying DA concentration and assembly time. The blue violin plot shows the distribution range of interlayer spacings for several samples fabricated under the same conditions. The black dot within the light-blue region denotes the mean interlayer spacing under the given condition. The distribution was obtained from statistical analysis of more than 50 independently prepared membranes under each condition. The top-left inset shows a representative distribution of interlayer spacing with a DA concentration of 0.03 mM and an assembly time of 60 min. **b**, Time-dependent growth of DA assemblies in composite GOMs prepared with 0.06 mM DA. Assembly size was statistically determined from top-view TEM images collected over several independent experiments. The error bars represent the s.d. The red dashed line represents the fitted trend line. Insets show TEM images after 10 min and 60 min of assembly. **c**, The cartoon illustration shows that both dimensions (top view and side view) increase simultaneously with extended assembly time. The light-blue spheres represent reactive molecules, and the grey-black hexagonal grids represent GO sheets. **d**, Attenuated total reflection-Fourier transform infrared spectroscopy analysis of the reaction between DA assemblies and oxygen-containing functional groups on GO surface (forming amido bond) in composite GOM with different reaction times. The black curve represents pristine GOM. The blue-to-purple curves correspond to reaction times of 0 h, 1 h, 6 h, 24 h and 48 h. Scale bars, 20 nm. a.u., arbitrary units.

to obstruct the spacing channels, as illustrated in the bottom panel of Fig. 1a.

Molecular dynamics simulations were performed to demonstrate the assembly of DA molecules within nanoconfined water and characterize their aggregation behaviour within GO sheets. Free-energy profiles reveal that DA molecules preferentially aggregate near oxygen-containing functional groups on GO (shown in Fig. 1b), and this trend remains valid across different interlayer spacings (Supplementary Fig. 5). Next, using density functional theory calculations (Extended Data Fig. 2), we found that the reactions between functional groups

of DA molecules and those on GO, as well as the reaction between two DA molecules, involve relatively high energy barriers compared with DA assembly and aggregation, further showing that the DA molecules tend to aggregate near the oxygen-containing groups on GO surface first before reacting with the oxygen-containing groups or undergoing self-polymerization, achieving the timescale separation of DA assembly process and reaction process as illustrated in Fig. 1a. In addition to primarily using DA as the model molecule for tuning interlayer spacing, we also found that other reaction pathways can serve as alternatives (Supplementary Fig. 6). During composite-GOM fabrication, the GOMs with thicknesses ranging from roughly 30 nm to several micrometres can be obtained. The GOMs that are too thin show poor mechanical strength and high defect density, whereas those that are too thick fail to effectively regulate the interlayer spacing. Therefore, a thickness range of 65–150 nm was selected in this study to ensure both structural integrity and spacing tunability (Fig. 1c). A transmission electron microscopy (TEM) image further reveals the well-controlled layer-by-layer stacking structure of the GO sheets (Fig. 1d). Furthermore, water immersion tests show that the GOMs retain their X-ray diffraction (XRD) characteristic peaks even after 30 days of immersion (bottom panel of Fig. 1e), confirming stable interlayer spacing in aqueous environment. By contrast, the XRD peak for the pristine GOM almost completely disappeared within 2 hours (upper panel of Fig. 1e), revealing structural instability induced by severe swelling. Moreover, the robustness of the composite GOM was verified by means of water flushing at a flow rate of 2 m s^{-1} (Fig. 1f). The composite GOM remained intact after 60 min of flushing, whereas the pristine GOM was easily washed away after only 10 s.

Tuning and stabilizing the GOM interlayer spacing

To systematically verify the controllability of the interlayer spacing in the GOMs, we performed large-scale fabrication under varied conditions, preparing more than 50 independent membrane samples for each set of parameters. All membrane samples were analysed using XRD, with interlayer spacing determined from the diffraction peak positions (2θ)[8]. As summarized in Fig. 2a, the interlayer spacing can be continuously adjusted across a range of 5.9–10.2 Å. For example, under conditions of 0.03-mM DA and 60-min assembly, the membranes showed a narrow interlayer spacing distribution between 6.32 Å and 6.64 Å across 50 tested samples made under identical fabrication conditions, with a standard deviation (s.d.) of 0.05 Å (inset of Fig. 2a). Similarly, for membranes with a target interlayer spacing of 10.0 Å, the calculated s.d. was 0.09 Å (Supplementary Fig. 7). These findings demonstrate that by controlling specific macroscopic preparation parameters, batches of composite GOMs with highly uniform interlayer spacing (s.d. less than 0.1 Å).

Whereas increasing the DA concentration (Supplementary Fig. 8) and extending assembly time (Fig. 2a) can enlarge the interlayer spacing, interlayer spacing beyond roughly 9 Å exceeds the diameters of hydrated ions in common salts[8], making it less relevant for ion sieving and desalination applications. Therefore, we focus on a controlled interlayer spacing range of 5.9 Å to 10.2 Å. To demonstrate the DA assembly between the GO sheets for adjusting the interlayer spacing, Fig. 2b presents the size evolution of assembled DA nanopillars over time, obtained from TEM images at a DA concentration of 0.06 mM as an example. Within 30 min, the lateral size of the assembled DA nanopillars increases to roughly 3.5 nm, corresponding to an interlayer spacing of 6.7 Å (Fig. 2a). After 60 min of assembly, the lateral size expands to roughly 5 nm, with a corresponding interlayer spacing of 7.0 Å (Fig. 2a). The representative TEM images in the insets visually depict DA assembly within GOMs at 10 min and 60 min, with further details provided in Supplementary Fig. 9. Although the top-view lateral size does not directly represent the height of the assembled DA nanopillars, both the lateral size and the nanopillar height (side view)

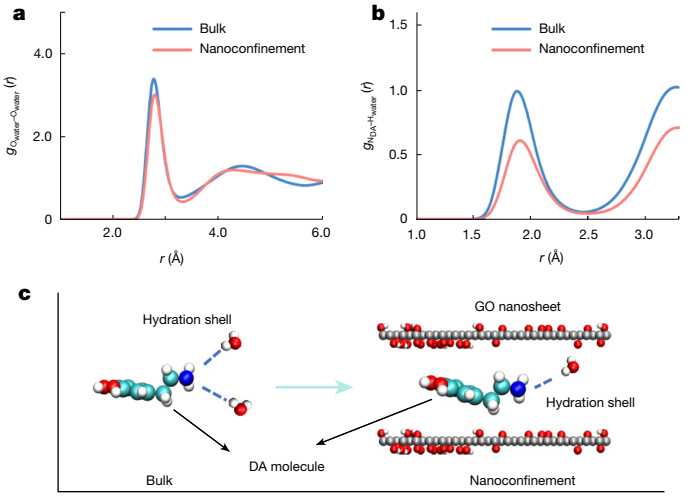

Fig. 3 | Mechanism of assembly of reactive molecules in nanoconfinement. **a**, RDF for O atoms of water molecules in the nanoconfined environment (pink line) and in bulk solution (blue line). $g(r)$ denotes the RDF, which describes the local atomic density at a distance, r, from a reference atom for an ideal uniform distribution. **b**, RDF for N atoms (of NH_2 group on DA molecules) and H atoms (of water molecules) in the nanoconfined environment (pink line) and in bulk solution (blue line). **c**, Schematic illustration of the hydration of DA in bulk solution (left-hand side of the panel) and in the nanoconfined environment (right-hand side of the panel), where the confined environment weakens the interactions between DA molecules and water. The red, white and blue spheres represent oxygen, hydrogen and nitrogen atoms, respectively, and the cyan and grey spheres represent carbon atoms in the DA molecules and GO nanosheets. The blue dashed lines represent hydrogen bonds.

increase simultaneously with extended assembly time, with the nanopillar height playing a key role in establishing well-defined interlayer spacing, as illustrated in Fig. 2c. Moreover, our molecular dynamics simulations demonstrate that when maintaining a constant density of assembled DA nanopillars, the average interlayer spacing increases with the number of DA molecules (Extended Data Fig. 3). Our DA assembly strategy also ensures a highly uniform interlayer spacing in the GOMs, as confirmed by conventional XRD and synchrotron-based grazing-incidence wide-angle X-ray scattering[17], as well as by measuring the spatial homogeneity of interlayer spacing for the GOMs (Extended Data Fig. 4 and Supplementary Fig. 10).

After achieving the desired assembly, the temperature is lowered to freeze the confined water into ice, allowing the subsequent slow reactions to fix the interlayer spacing and stabilize the structure. As shown in Fig. 2d, the attenuated total reflection-Fourier transform infrared spectroscopy reveals the reactions between PDA and GO, which stabilize the interlayer spacing and enhances the structural strength of composite GOMs. The formation of amido bonds (–NHOC–) increases progressively over 24 hours, indicating continuing reactions between the amine groups ($-NH_2$) in DA molecules and the carboxyl groups (–COOH) on the GO surface. This reaction plays a crucial role in strengthening the interactions between the GO sheets[6]. In addition, the self-polymerization of DA is indicated by the GOM turning dark brown, signalling the formation of PDA[18], as shown in Supplementary Fig. 11. This polymerization process requires more than 24 hours to complete under low-temperature conditions.

Mechanism of interlayer spacing regulation

Figure 3 illustrates the detailed mechanism underlying the nanoconfined water-induced DA assembly at the molecular level. To elucidate the intrinsic mechanism, we analysed the radial distribution function (RDF) for O_{water} of water molecules (Fig. 3a), and the RDF for nitrogen

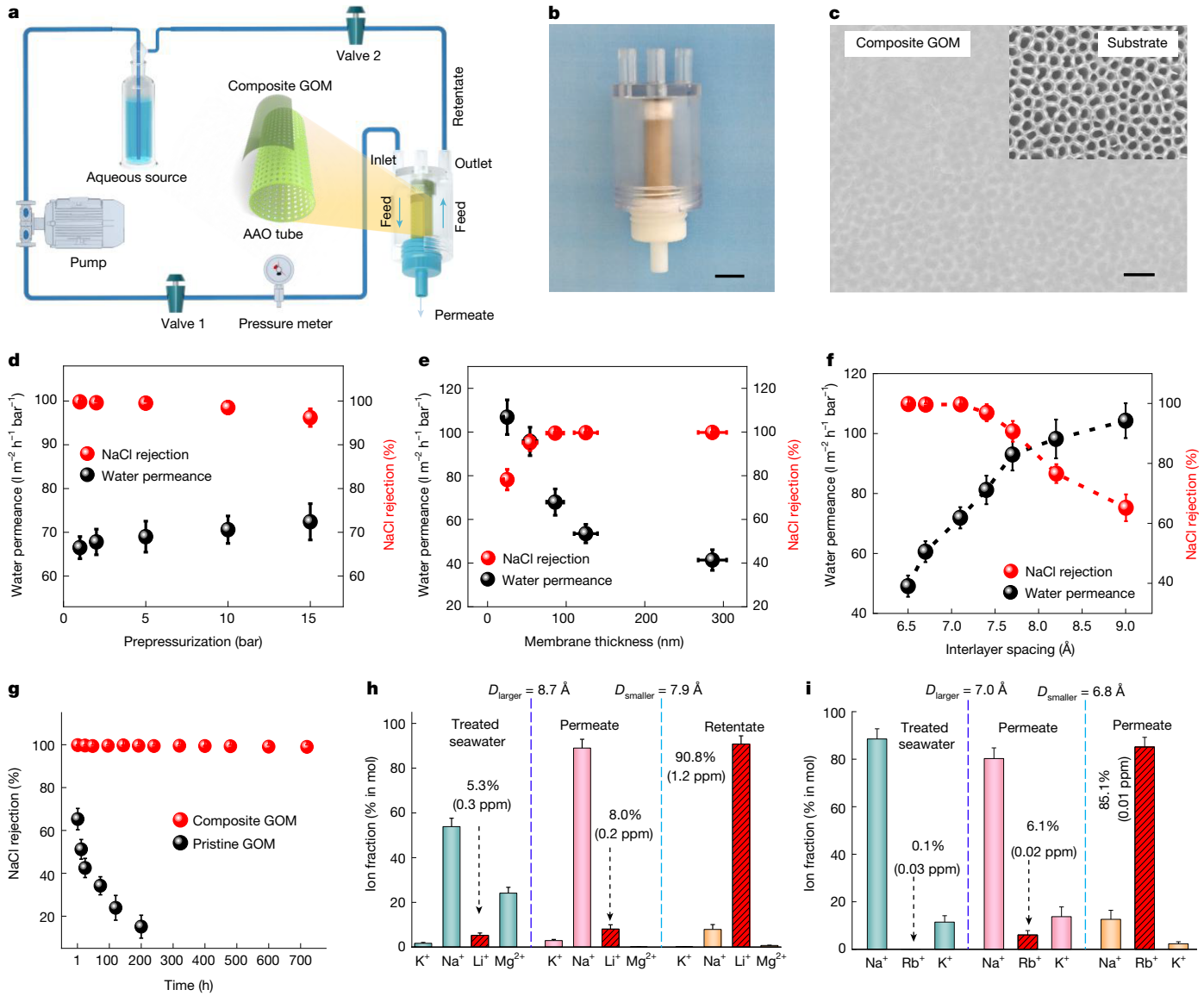

Fig. 4 | The composite-GOM cross-flow filtration device for water permeation, NaCl rejection and cation-sieving performance. a, Schematic of the GOM cross-flow filtration device. **b**, Photograph of the filtration device with the integrated composite GOM. **c**, Scanning electron microscopy image of the GOM on an anodic alumina membrane. **d**–**f**, Water permeance and NaCl rejection as functions of prepressurization pressure (**d**), membrane thickness (**e**) and interlayer spacing (**f**) in aqueous environments. Black and red sphere symbols denote water permeance and NaCl rejection, respectively. Data are means from more than ten measurements; error bars indicate s.d. **g**, The NaCl rejection plotted against operation time for the GOMs (red spheres) and pristine GOMs (black spheres) under cross-flow conditions. Every data point is averaged over five measurements, and error bars indicate the s.d. **h**,**i**, For sieving Li^+ (**h**) and Rb^+ (**i**), red bars with black diagonal stripes denote the Li^+ and Rb^+ ion fractions. In **h**, the composite GOMs have interlayer spacings of D_{larger} = 8.7 Å (blue dashed line) and $D_{smaller}$ = 7.9 Å (light-blue dashed line), respectively. In **i**, the composite GOMs have interlayer spacings of D_{larger} = 7.0 Å (blue dashed line) and $D_{smaller}$ = 6.8 Å (light-blue dashed line), respectively. For **h** and **i**, the bar height represents the mean of more than ten independent measurements, and error bars show the s.d. AAO, anodic aluminium oxide. Scale bars, 1 cm (**b**); 1 µm (**c**).

atoms of the NH_2 group on DA and H_{water} of water molecules (Fig. 3b), within both GO nanoconfinement and bulk solution. The intensity of RDF peaks serves as a quantitative measure of the interaction strength between a molecule (either water or DA) and its surrounding water molecules. In comparison to DA in bulk water, the H atoms of the NH_2 group on DA within the nanoconfinement show weaker interactions with water molecules (Supplementary Fig. 12). Conversely, the RDFs of O_{water}···O_{water} in confined water and bulk water are nearly identical, indicating that water–water interactions in the nanoconfinement are comparable in strength to those in bulk water. As shown in Fig. 3c, water–DA interactions in the nanoconfinement are weaker than in bulk water, whereas water–water interactions remain similar. This weaker interaction in the nanoconfinement promotes the aggregation of DA molecules, thereby lowering the system's overall energy. In other words, the nanoconfinement induces DA molecule assembly, which promotes the formation of the PDA structure that controls the interlayer spacing. This diffusion and reaction pathway is key to effectively tuning molecular aggregation and membrane properties.

Practical applicability of fabricated GOM devices

We constructed a cross-flow filtration apparatus (Fig. 4a,b) using the composite GOMs for desalination and ion sieving from pretreated seawater (Methods). Using this setup, we systematically examined water permeance and NaCl rejection as a function of prepressurization pressure, membrane thickness and interlayer spacing of the GOMs with

a 2,000 ppm NaCl solution (Fig. 4d–f). As shown in Fig. 4d, before water permeance and NaCl rejection tests, we prepressurized the membrane with water hydraulic pressure to compact the GOM and evaluate its pressure resistance (Supplementary Fig. 13). Note that the pressure on the *x* axis of Fig. 4d corresponds to this prepressurization stage, not the operating pressure during desalination. After 10-bar prepressurization, the GOM maintained a NaCl rejection rate of 98.5% under an operating pressure of 5 bar (Fig. 4d).

In addition, the thickness of the GOMs influences both the water permeance and NaCl rejection (Fig. 4e). An optimal thickness of roughly 90 nm (Figs. 1c and 4e) balances structural strength, water permeance and salt rejection (details in Supplementary Fig. 14). As the interlayer spacing increases from 6.5 Å to 9.0 Å (measured in aqueous environment), water permeance rises from 49.1 l m^{-2} h^{-1} bar^{-1} to 104.3 l m^{-2} h^{-1} bar^{-1}, whereas NaCl rejection drops from 99.8% to 65.2% (Fig. 4f). Notably, the GOMs show a stable NaCl rejection as high as 99.0% over 700 hours (red-ball markers in Fig. 4g). By contrast, the pristine GOMs show a rapid decline from 65.3% to 15.1%, due to uncontrollable swelling (black-ball markers in Fig. 4g). These results demonstrate the long-term desalination applicability of the composite GOMs. To meet seawater desalination requirements[9,13,19–22], the GOM showed a NaCl rejection rate of 99.4% over 16 days, and after 30 days of continuous operation, the rejection remained 99.0%, with a roughly 0.4% decline, demonstrating stable performance (Fig. 4g). A water permeance of 67.9 l m^{-2} h^{-1} bar^{-1} was maintained throughout the 30-day test. The efficient water transport arises from the formation of PDA nanopillars at oxidized regions on the GO surface, while leaving abundant graphene-based channels for water permeation (Extended Data Fig. 5 and Supplementary Fig. 15). Furthermore, the membranes show robust separation performance under high-salinity conditions, suggesting potential for ion separation and water recovery from highly concentrated saline solutions (Supplementary Fig. 16).

Next, we used the designed filtration device and operational setup (Fig. 4a–c and Supplementary Fig. 13) to evaluate the ion-sieving performance of the composite GOMs. Extended Data Fig. 6 shows the permeation rates of various salts (RbCl, KCl, NaCl, LiCl, $CaCl_2$ and $MgCl_2$) with different hydrated ionic diameters. Extended Data Fig. 7 shows that ion hydration-size and hydration-energy differences can guide the selection of suitable interlayer spacings for selective ion separation. By matching the hydrated diameter of Li^+, the GOMs with interlayer spacing of D_{larger} = 8.7 Å and $D_{smaller}$ = 7.9 Å efficiently separate Li^+ from pretreated seawater (Fig. 4h), increasing its molar ratio from 5.3% to 90.8%. In lithium-ion battery production, both Li^+ and Mg^{2+} can form precipitates with carbonate (CO_3^{2-})[23–26], whereas high-concentration Na^+ may also coprecipitate with Li^+[27–29]. Therefore, effective separation of Li^+ from Mg^{2+} and Na^+ is crucial. The GOMs achieve selectivity factors of Li^+/Mg^{2+} = 631 and Na^+/Li^+ = 148, respectively, significantly enhancing the purity of the recovered Li^+. Rubidium (Rb^+) is essential in various high-tech applications, yet membrane separation of Rb^+ is extremely challenging due to its minimal hydrated diameter difference (less than 0.1 Å) with potassium (K^+)[30]. Using a dual-membrane configuration: first, the GOM with D_{larger} = 7.0 Å preferentially transports Rb^+ while suppressing K^+ permeation, balancing enrichment and flux (Extended Data Fig. 8); then, the GOM with $D_{smaller}$ = 6.8 Å selectively rejects K^+, yielding highly enriched Rb^+ in the permeate solution (Fig. 4i). As a result, the Rb^+ concentration increases from 0.1% to 85.1%, achieving a Rb^+/K^+ selectivity factor of 5,320, significantly outperforming conventional precipitation and adsorption-based extraction methods[30].

Although the hydrated diameters of K^+, Li^+ and Rb^+ all exceed the corresponding channel sizes of the GOMs (interlayer spacing minus the thickness of the carbon layer) as shown in Fig. 4h,i and Extended Data Fig. 7, the prevailing consensus of ion permeation is that ions undergo partial dehydration when traversing the subnanochannels[8,31–33]. To validate this mechanism, we performed molecular dynamics simulations using K^+ permeating through a membrane with an interlayer spacing of 7.0 Å (channel sizes roughly 3.6 Å) as a representative case. The results show that on entering the subnanochannels, K^+ partially sheds its hydration shells, leading to a notable reduction in hydration number and effectively lowering its apparent hydrated size (Extended Data Fig. 9). Structural snapshots (Extended Data Fig. 9c) visually demonstrate this partial dehydration process, explaining how hydrated ions can permeate even when their apparent hydrated diameters exceed the channel size[8,31,34–36]. Furthermore, the order of dehydration energies for different ions passing through the GOMs with the same interlayer spacing, as obtained from theoretical calculations, is closely aligned with the experimentally observed trend in ion selectivity[8,32].

Discussion

In summary, we report a new synthetic method for making a new class of PDA-pillared GOMs with tunable and stable interlayer spacing, featuring controllable interlayer spacings down to 5.9 Å in the dry state, and the capacity to separate the hydrated metal ions differing in size by less than 0.1 Å in aqueous environments. The interlayer spacing remains highly stable over long periods under aqueous conditions, enabling sustained seawater desalination and ion separation. Such a control is achieved by implementing an assembly and/or reaction time-separation strategy. During the assembly, DA molecules form nanopillar structures at the sites of oxygen-containing functional groups on the GO surface, enabling the subnanoscale adjustment of the interlayer spacing while minimally occupying carbon-rich regions for fast water and/or ion transport. Further, the self-polymerized DA nanopillar array bonding with GO sheets within the membrane stabilizes both the interlayer spacing and composite-GOM structure. The tunability of the interlayer spacing allows us to select a specific interlayer spacing for sieving of target ions. The theoretical calculations provide a mechanistic understanding on how the composite GOMs can achieve the ion selectivity by taking advantage of different degrees of partial dehydration for ions with different hydration diameters. Overall, this joint experimental and theoretical study not only extends the field of nanoconfined water solutions from fundamental scientific research to practical engineering applications, but also offers a feasible path towards scaling-up applications for generic ion selection and desalination.

Online content

Any methods, additional references, Nature Portfolio reporting summaries, source data, extended data, supplementary information, acknowledgements, peer review information; details of author contributions and competing interests; and statements of data and code availability are available at https://doi.org/10.1038/s41586-026-10765-4.

1. Mi, B. Scaling up nanoporous graphene membranes. *Science* **364**, 1033–1034 (2019).
2. Akbari, A. et al. Large-area graphene-based nanofiltration membranes by shear alignment of discotic nematic liquid crystals of graphene oxide. *Nat. Commun.* **7**, 10891 (2016).
3. Perreault, F., Fonseca de Faria, A. & Elimelech, M. Environmental applications of graphene-based nanomaterials. *Chem. Soc. Rev.* **44**, 5861–5896 (2015).
4. Joshi, R. K. et al. Precise and ultrafast molecular sieving through graphene oxide membranes. *Science* **343**, 752–754 (2014).
5. Nair, R. R., Wu, H. A., Jayaram, P. N., Grigorieva, I. V. & Geim, A. K. Unimpeded permeation of water through helium-leak-tight graphene-based membranes. *Science* **335**, 442–444 (2012).
6. Zhang, M. et al. Molecular bridges stabilize graphene oxide membranes in water. *Angew. Chem. Int. Ed.* **59**, 1689–1695 (2019).
7. Chen, L. et al. Ion sieving in graphene oxide membranes via cationic control of interlayer spacing. *Nature* **550**, 380–383 (2017).
8. Abraham, J. et al. Tunable sieving of ions using graphene oxide membranes. *Nat. Nanotechnol.* **12**, 546–550 (2017).
9. Jiang, Z., Karan, S. & Livingston, A. G. Water transport through ultrathin polyamide nanofilms used for reverse osmosis. *Adv. Mater.* **30**, 1705973 (2018).
10. Epsztein, R., DuChanois, R. M., Ritt, C. L., Noy, A. & Elimelech, M. Towards single-species selectivity of membranes with subnanometre pores. *Nat. Nanotechnol.* **15**, 426–436 (2020).

11. Elimelech, M. & Phillip, W. A. The future of seawater desalination: energy, technology, and the environment. *Science* **333**, 712–717 (2011).
12. Lim, Y. J., Goh, K. & Wang, R. The coming of age of water channels for separation membranes: from biological to biomimetic to synthetic. *Chem. Soc. Rev.* **51**, 4537–4582 (2022).
13. Zhang, W.-H. et al. Graphene oxide membranes with stable porous structure for ultrafast water transport. *Nat. Nanotechnol.* **16**, 337–343 (2021).
14. Zhou, K. G. et al. Electrically controlled water permeation through graphene oxide membranes. *Nature* **559**, 236–240 (2018).
15. Huang, H. et al. Ultrafast viscous water flow through nanostrand-channelled graphene oxide membranes. *Nat. Commun.* **4**, 2979 (2013).
16. Hung, W.-S. et al. Cross-linking with diamine monomers to prepare composite graphene oxide-framework membranes with varying d-spacing. *Chem. Mater.* **26**, 2983–2990 (2014).
17. Andreeva, D. V. et al. Two-dimensional adaptive membranes with programmable water and ionic channels. *Nat. Nanotechnol.* **16**, 174–180 (2021).
18. Cihanoglu, A., Schiffman, J. D. & Altinkaya, S. A. Ultrasound-assisted dopamine polymerization: rapid and oxidizing agent-free polydopamine coatings on membrane surfaces. *Chem. Commun.* **57**, 13740–13743 (2021).
19. Yan, H. et al. The porous structure of the fully-aromatic polyamide film in reverse osmosis membranes. *J. Membr. Sci.* **475**, 504–510 (2015).
20. Meng, N. et al. A low-pressure GO nanofiltration membrane crosslinked via ethylenediamine. *J. Membr. Sci.* **548**, 363–371 (2018).
21. Morelos-Gomez, A. et al. Effective NaCl and dye rejection of hybrid graphene oxide/graphene layered membranes. *Nat. Nanotechnol.* **12**, 1083–1088 (2017).
22. Hu, M. & Mi, B. Enabling graphene oxide nanosheets as water separation membranes. *Environ. Sci. Technol.* **47**, 3715–3723 (2013).
23. Hong, S. et al. Precision ion separation via self-assembled channels. *Nat. Commun.* **15**, 3160 (2024).
24. He, R. et al. Polyelectrolyte-based nanofiltration membranes with exceptional performance in Mg^{2+}/Li^{+} separation in a wide range of solution conditions. *J. Membr. Sci.* **663**, 121027 (2022).
25. Peng, H., Hu, Y., Li, S., Rao, J. & Zhao, Q. Sulfonium-polyamide membranes for high flux Mg^{2+}/Li^{+} separation. *J. Membr. Sci.* **674**, 121515 (2023).
26. Chen, K. et al. Dual-electric layer nanofiltration membranes based on polyphenol/PEI interlayer for highly efficient Mg^{2+}/Li^{+} separation. *J. Membr. Sci.* **660**, 120860 (2022).
27. Liu, C. et al. Lithium extraction from seawater through pulsed electrochemical intercalation. *Joule* **4**, 1459–1469 (2020).
28. Butylskii, D. Y. et al. Review of recent progress on lithium recovery and recycling from primary and secondary sources with membrane-based technologies. *Desalination* **586**, 117826 (2024).
29. Liu, Y. et al. Pillared laminar vermiculite membranes with tunable monovalent and multivalent ion selectivity. *Adv. Mater.* **37**, e2417994 (2025).
30. Chen, X. & Hu, W. Direct and efficient in situ rubidium extraction from potassium chloride salts. *Nat. Sustain.* **7**, 1672–1680 (2024).
31. Chen, W. et al. Cascade-heterogated biphasic gel iontronics for electronic-to-multi-ionic signal transmission. *Science* **382**, 559–565 (2023).
32. Esfandiar, A. et al. Size effect in ion transport through angstrom-scale slits. *Science* **358**, 511–513 (2017).
33. Xu, R., Kang, Y., Zhang, W., Pan, B. & Zhang, X. Two-dimensional MXene membranes with biomimetic sub-nanochannels for enhanced cation sieving. *Nat. Commun.* **14**, 4907 (2023).
34. Liao, S. et al. Theoretical framework for confined ion transport in two-dimensional nanochannels. *Nat. Commun.* **16**, 6675 (2025).
35. Hou, Y. et al. Artificial cation-chloride co-transporters for chloride-facilitated lithium/magnesium separation. *Angew. Chem. Int. Ed. Engl.* **64**, e202504259 (2025).
36. Trushin, M., Andreeva, D. V., Peeters, F. M. & Novoselov, K. S. Structure and flow of low-dimensional water. *Nat. Rev. Phys.* **7**, 502–513 (2025).

Publisher's note Springer Nature remains neutral with regard to jurisdictional claims in published maps and institutional affiliations.

Open Access This article is licensed under a Creative Commons Attribution-NonCommercial-NoDerivatives 4.0 International License, which permits any non-commercial use, sharing, distribution and reproduction in any medium or format, as long as you give appropriate credit to the original author(s) and the source, provide a link to the Creative Commons licence, and indicate if you modified the licensed material. You do not have permission under this licence to share adapted material derived from this article or parts of it. The images or other third party material in this article are included in the article's Creative Commons licence, unless indicated otherwise in a credit line to the material. If material is not included in the article's Creative Commons licence and your intended use is not permitted by statutory regulation or exceeds the permitted use, you will need to obtain permission directly from the copyright holder. To view a copy of this licence, visit http://creativecommons.org/licenses/by-nc-nd/4.0/.

© The Author(s) 2026

Methods

Preparation of GO sheets with controllable lateral sizes

Aqueous dispersions of GO with broad size distributions, synthesized by means of a modified Hummer's method[37], were purchased from Nanjing XFNANO Materials Tech Co., Ltd. Temperature-controlled fractionated centrifugation was used to separate the polydisperse GO dispersions into several distinct size groups. To measure the lateral size of the GO nanosheets, droplets of the GO dispersion were deposited on silicon wafers and air dried. Lateral size distributions were determined from atomic force microscopy images (Supplementary Fig. 17) by analysing more than 500 nanosheets per sample. The average lateral size of irregularly shaped GO nanosheets was calculated as the mean of their largest and smallest transverse widths. The sorted GO fractions were immersed in water and stored at 4 °C to prevent aggregation. For this study, the roughly 2-μm GO size fraction was selected on the basis of its optimal performance characteristics (Supplementary Fig. 18).

Preparation of GO with varying oxidation degrees

GOs with different oxidation levels were prepared using a modified Hummer's method[37]. Four GO samples with varying degrees of oxidation, covering a wide range of oxygen content, were synthesized by adjusting the amount of oxidant ($KMnO_4$) and oxidation time during the preparation process. It was observed that freshly prepared GO samples showed non-uniform sizes, with smaller GO sheets generally having higher oxidation degree. A patchwork GOM with fewer oxygen-containing functional groups showed higher permeability at the same interlayer spacing, whereas membranes with strong binding pillars required appropriate oxidation to provide robust linking and support, preventing swelling and collapse. On the basis of these characteristics, membranes with 25.4% oxygen content oxidation showed optimal performance in composite GOMs, compared with the typical 30.6% oxygen content (Supplementary Fig. 19). Furthermore, the GOs with varying oxidation degrees were subjected to fractionated centrifugation before membrane preparation to ensure optimal performance in composite GOMs.

Preparation of GOMs

The prepared size-graded GO sheets were diluted to a concentration of 2 μg ml^{-1}. The diluted suspension was then filtered under a vacuum pressure of roughly 0.01–0.02 MPa through microporous substrates (cellulose, nylon, polyethersulfone or anodized aluminium oxide and so on) or alumina ceramic tubes, all with a pore size of roughly 0.22 μm, to form GO films. In the experiment, the operation with lower concentration and lower vacuum pressure provided sufficient time for the GO sheets to spread uniformly, resulting in flat and consistent membrane. The GOMs were subsequently freeze dried using a freeze dryer (LGJ-10E, Sihuankeyi Co., Ltd).

Preparation of the composite GOMs

The freeze-dried GOMs were immersed in aqueous solutions of reactive molecules (for example, DA) at various concentrations (0.03 mM, 0.06 mM, 0.13 mM, 0.33 mM, 0.65 mM and 1.3 mM, pH 7.5) for 1–3 min (Supplementary Fig. 1). The solution volume was carefully controlled to infiltrate the membrane sufficiently while preventing rapid swelling into disordered, stacked GO sheets. The membranes were then frozen at temperatures below −50 °C. Unlike traditional immersion strategies that result in uncontrolled swelling, the frozen surrounding bulk ice extracted some liquid water in confinement from the GOM interlayers, thereby minimizing the initial interlayer spacing. This process was followed by annealing below the bulk ice freezing point (for example, −10 °C) for various annealing times to achieve the desired GOM interlayer spacing. Then, the GOMs were cooled to below −30 °C for the reaction process. The GOMs were subsequently freeze dried to obtain the PDA-crosslinked GOM (composite GOM).

Building on this approach, the mixed solution of benzene-1,2,4,5-tetramine (P) and benzene-1,3,5-tricarboxylic acid (A) in a 3:2 ratio was used to fabricate the poly-PA-crosslinked GOM. During the reaction, the P and A molecules underwent copolymerization. For freeze-dried GOM treated with aqueous acrylamide solutions, the membrane was further exposed to ultraviolet light for 1 h, yielding poly-AM-crosslinked GOM membranes (Supplementary Fig. 6). In our approach, we introduced this mechanism to achieve the separation of reactive molecular assembly and subsequent reactions. It prevented the imprecise spacing regulation and channel blockage from excessive reacted molecules to flux reduction, which can possibly arise from simultaneous assembly and reaction or from relying solely on chemical reactions for interlayer stabilization[6].

PVA-modified anodic aluminium oxide ceramic tube surface

Polyvinyl alcohol (PVA) was dissolved in water and heated to 95 °C to prepare a 1 wt% aqueous solution. Ceramic tubes were immersed in the PVA solution for 1 h to deposit the PVA on the substrate surface. The tubes were then rinsed with deionized water and left to dry naturally at room temperature for 12 h, resulting in PVA-modified ceramic tubes. This modification improved the adhesion between the ceramic substrate and the GO-based membrane.

Configuration of filtration device with the GOMs

The filtration device consisted of a flexible, flat and reinforced composite GOM securely adhered to a cylindrical hydrophilic-modified ceramic tube for mechanical stability of composite GOMs. The feed solution was pumped through the composite-GOM filtration system, with the retentate being recycled while the permeate water was collected, as shown in Fig. 4a.

Low-temperature differential scanning calorimetry measurements

We conducted low-temperature differential scanning calorimetry measurements on membrane-GOMs with different interlayer spacings to determine the freezing behaviour of nanoconfined water. As shown in Extended Data Fig. 1, differential scanning calorimetry thermograms showed distinct crystallization peaks as the temperature decreased from −10 °C to −30 °C. On the basis of the precedent set in the literature[38], the higher-temperature peak was attributed to bulk-like water freezing, whereas the lower-temperature peak corresponded to the freezing of confined water. Compared with the exothermic peak of bulk water freezing, the exothermic peak of confined water freezing was much smaller, with a reduced peak area. Therefore, to better show the freezing temperature of confined water in membranes with different interlayer spacings, we have amplified the confined water crystallization peak (Extended Data Fig. 1a). The freezing temperature of confined water decreased as the interlayer spacing decreased, as shown in Extended Data Fig. 1b. Moreover, in some cases (for example, between −5 °C and −15 °C), only a single broad peak was observed, which we attributed to the overlap of bulk and confined water crystallization transitions (not shown here). In addition, the limited exothermic heat released during the crystallization of confined water resulted in a melting process that was much smaller compared with bulk ice melting. As a result, the melting peak of confined ice was overshadowed by the melting peak of bulk ice.

In situ XRD for frozen samples

The frozen GOMs were placed in a sealed temperature-controlled system integrated with XRD apparatus (PANalytical) for analysis. The interlayer spacing was measured by using powder XRD with the angular range of 3–80° (2θ) at a scanning speed of 10° min^{-1} with the Cu Kα radiation (wavelength λ = 1.54056 Å).

Measurement of the interlayer spacing of GOMs

The interlayer spacing was measured by using powder XRD with the angular range of 3–30° (2θ) at a scanning speed of 5° min^{-1} by using an

X-ray diffractometer (PANalytical) and the wavelength of the Cu Kα radiation (λ = 1.54056 Å). The Bragg equation $2d\sin\theta = n\lambda$ was used to calculate the interlayer spacing.

Synchrotron radiation source for testing GOMs in dry state

The synchrotron grazing-incidence wide-angle X-ray scattering two-dimensional (2D) patterns were collected on the BL14B1 and BL16B1 beamlines at Shanghai Synchrotron Radiation Facility, using a fixed wavelength of 1.2398 Å (10 keV), an exposure time of 200 s and an incident angle of 0.2°. The relationship between the 2θ and interlayer spacing was calculated from the grazing-incidence wide-angle X-ray scattering 2D patterns through the open access software of FIT2D.

Electron microscopy characterization

GO dispersions were deposited onto TEM grids on a filter paper. DA solutions at varying concentrations (0.03 mM, 0.06 mM, 0.13 mM, 0.33 mM, 0.65 mM and 1.3 mM) were subsequently added to infiltrate the GO layer on the grids. Then we followed the method of preparing composite-GOM samples to first rapidly freeze the GOMs, followed by annealing to obtain the target composite GOMs for TEM imaging. High-resolution TEM images were obtained at the acceleration voltage of 200 kV on a JEM-2100F electron microscope.

Moreover, some morphologies images were examined at 5 kV using a field-emission scanning electron microscope instrument (Hitachi S-4800).

Evaluation of membrane performance

The performance of the GOMs was evaluated using a cylinder-shaped filtration cell for testing the composite GOM supported by ceramic substrates with an effective membrane area of 10.6 cm^2 shown in Supplementary Figs. 13 and 20. For the cylinder-shaped filtration cell, taking permeation tests of 2,000 ppm NaCl as an example, the composite GOM was placed on the cylindrical ceramic substrate, with the composite-GOM layer facing the feed NaCl solution. The NaCl aqueous solution was pumped into the cell through the inlet as the feed solution and exited through the outlet as the retentate. After the system reaching steady-state, the permeates were collected after passing through the composite GOM was recorded as the permeate solution for subsequent analysis. The process was conducted at room temperature, with an operating pressure of 5 bar and a cross-flow rate of 50 l h^{-1}.

The water permeance (J_w) was determined by means of the equation:

$$J_w = \frac{\Delta V}{\Delta t \times A \times \Delta P}$$

where J_w is the water permeance (l m^{-2} h^{-1} bar^{-1}), ΔV is the volume of permeate solution (in l), Δt is the test time (h), A is the effective membrane area (m^2) and ΔP is the transmembrane pressure difference (bar).

The single salt rejection (R) was calculated by using the equation[7,39]:

$$R = 1 - \frac{C_{permeate}}{C_{feed}} \times 100\%$$

where $C_{permeate}$ is the concentration of a specific target salt in the permeate solution and C_{feed} is the concentration of the same target salt in the feed solution. The conductivity of the permeate solution was measured using a conductivity meter (Mettler-Toledo), and ion chromatography (Thermo Fisher Scientific).

The salt concentration can be calculated using the equation:

$$C = \frac{\kappa}{\Lambda_m}$$

where C is the salt concentration, κ is the measured conductivity and Λ_m is the molar conductivity. Within the salt concentration range tested in this work, the conductivity showed a linear relationship with concentration, thus allowing the salt rejection to be determined from conductivity measurements.

The selectivity coefficient, $S_{A,B}$, for ion A over ion B was quantitatively determined using equation:

$$S_{A,B} = \frac{\frac{C_{permeate,A}}{C_{feed,A}}}{\frac{C_{permeate,B}}{C_{feed,B}}}$$

where, $C_{feed,A}$ and $C_{feed,B}$ correspond to the concentrations of ion A and ion B in the feed solution, whereas $C_{permeate,A}$ and $C_{permeate,B}$ represent the concentrations of ion A and ion B in the permeate. Specifically, In Fig. 4h,i, only the main metal-ion species are presented for clarity. The total ion fraction does not sum to unity because Ca^{2+} are not shown. Metal-ion concentrations were measured using inductively coupled plasma spectroscopy (iCAP RQ, Thermo Fisher Scientific). At the same time, anion concentrations were determined by ion chromatography (Thermo Fisher Scientific).

The ion permeation rate (J_i) was calculated according to the equation:

$$J_i = \frac{V \times C_{ion}}{A \times \Delta t}$$

where V is the effective volume of the permeate solution, C_{ion} is the ion concentration in the permeate side, A is the effective membrane area and Δt is the permeation time.

In addition, we conducted ion-sieving and permeation tests of pretreated seawater (as a feed solution, seawater was obtained from China Bohai). In this work, after pretreatment, the Li^+ concentration reached roughly 0.3 ppm and the treated seawater was used as the feed solution in Fig. 4h. Also, when the Rb^+ concentration reached roughly 0.03 ppm, it was used as the feed solution in Fig. 4i. Therefore, the membrane performance discussed in this work was evaluated from a defined feed solution obtained after pretreatment, rather than directly from raw seawater.

Surface zeta potential measurements

Zeta potentials of the membrane surface were calculated by streaming potential measurements by an electrokinetic analyser (Anton Paar, SurPASS), in which 1 mM of KCl solution under neutral conditions was passed over the membrane surface.

To systematically evaluate the role of surface charge in ion separation within composite GOMs, we measured the surface zeta potentials of composite GOMs with different interlayer spacings[40]. As shown in Extended Data Fig. 10, despite significant variations in interlayer spacing, the zeta potential values remained largely consistent across all membranes, indicating that the confinement-driven molecular assembly does not alter the membrane surface charge characteristics. The key finding was that despite similar surface charge states, membranes with different interlayer spacings showed distinct metal-ion separation performance (Extended Data Fig. 6). This comparative result confirmed that surface charge did not play a dominant role in the ion-sieving process within composite GOM.

Atomic force microscopy characterizations

The Multimode 8 (Bruker) was used to characterize the morphology and size of GO sheets.

Optical characterization

Digital photographs were taken with a Nikon eclipse LVDIA-N microscope equipped with a CCD (DS-Ri2).

Molecular dynamics simulations

The simulation system contained 2 GO sheets, 4 DA molecules and about 1,800 water molecules in a box with the dimensions 50.92 ×

50.40×30.00 Å^3 (Supplementary Fig. 21). The periodic boundary conditions were applied to all three dimensions in the simulation. To simulate the original graphene region and the GO region, we reduced the oxidation degree of GO sheets with a formula of $C_{20}O_1(OH)_1$, which contained 39 hydroxyl groups (−OH) and 39 epoxy groups (−O−). In the simulation, the C atoms were fixed in the *y* direction to keep the interlayer spacing at 10 Å. The simulation was carried out in the constant-temperature-volume (NVT) ensemble with a time step of 1 fs. The temperature was kept at 260 K by a velocity-rescale thermostat[41]. Each simulation was run for 40 ns, with the last 30 ns being used for data analysis. An all-atom optimized potential for liquid simulations was used for GO sheets and DA molecules[42], and the TIP4P/2005 water model was applied for water molecules[43]. Lennard–Jones and Coulomb potentials were used to simulate non-bonding interactions, with the electrostatic interactions being calculated using the particle mesh Ewald summation method[44] and a 10-Å real-space cut-off for non-bonding interactions. The LINCS algorithm was used to constrain covalent bonds and angles[45]. The free-energy profile of DA molecules confined in GO nanosheets was computed using the umbrella sampling method. Free energies were estimated using the weighted histogram analysis method[46]. All classical molecular dynamics simulations were conducted using the GROMACS package[47]. The program VMD was used for data analysis and molecular graphics[48].

Density functional theory calculations

All density functional theory calculations were performed using Gaussian 09 software[49]. The electronic structural optimization and reaction barrier calculation were performed based on an implicit water solvent model at the B3LYP/6-311++G** level[50] with Grimme's dispersion corrections[51]. The hydration energies of ion-water clusters (ion-$(H_2O)_6$) for Rb^+, K^+, Na^+ and Li^+ were further calculated at the B3LYP level with a mixed basis set: the Stuttgart/Dresden effective core potential (SDD) pseudopotential for the cations and the 6-311++G** basis set for water molecules. Basis set superposition error corrections were applied to the hydration-energy calculations.

Data availability

All data generated or analysed during this study are included in the Article and its Supplementary Information. Source data are provided with this paper.

37. Xu, Y., Bai, H., Lu, G., Li, C. & Shi, G. Flexible graphene films via the filtration of water-soluble noncovalent functionalized graphene sheets. *J. Am. Chem. Soc.* **130**, 5856–5857 (2008).
38. Cuadrado-Collados, C. et al. Freezing/melting of water in the confined nanospace of carbon materials: effect of an external stimulus. *Carbon* **158**, 346–355 (2020).
39. Heiranian, M., Fan, H., Wang, L., Lu, X. & Elimelech, M. Mechanisms and models for water transport in reverse osmosis membranes: history, critical assessment, and recent developments. *Chem. Soc. Rev.* **52**, 8455–8480 (2023).
40. Childress, A. E. & Elimelech, M. Relating nanofiltration membrane performance to membrane charge (electrokinetic) characteristics. *Environ. Sci. Technol.* **34**, 3710–3716 (2000).
41. Bussi, G., Donadio, D. & Parrinello, M. Canonical sampling through velocity rescaling. *J. Chem. Phys.* **126**, 014101 (2007).
42. Jorgensen, W. L. & Tirado-Rives, J. The OPLS [optimized potentials for liquid simulations] potential functions for proteins, energy minimizations for crystals of cyclic peptides and crambin. *J. Am. Chem. Soc.* **110**, 1657–1666 (1988).
43. Abascal, J. L. F. & Vega, C. A general purpose model for the condensed phases of water: TIP4P/2005. *J. Chem. Phys.* **123**, 234505 (2005).
44. Darden, T., York, D. & Pedersen, L. Particle mesh Ewald: an N·log(N) method for Ewald sums in large systems. *J. Chem. Phys.* **98**, 10089–10092 (1993).
45. Hess, B., Bekker, H., Berendsen, H. J. C. & Fraaije, J. G. E. M. LINCS: a linear constraint solver for molecular simulations. *J. Comput. Chem.* **18**, 1463–1472 (1997).
46. Kumar, S., Rosenberg, J. M., Bouzida, D., Swendsen, R. H. & Kollman, P. A. The weighted histogram analysis method for free-energy calculations on biomolecules. I. The method. *J. Comput. Chem.* **13**, 1011–1021 (2004).
47. Pronk, S. et al. GROMACS 4.5: a high-throughput and highly parallel open source molecular simulation toolkit. *Bioinformatics* **29**, 845–854 (2013).
48. Humphrey, W., Dalke, A. & Schulten, K. V. M. D. Visual molecular dynamics. *J. Mol. Graphics* **14**, 33–38 (1996).
49. Frisch, M. J. et al. Gaussian 09, Revision D.01 (Gaussian, 2013).
50. Stephens, P. J., Devlin, F. J., Chabalowski, C. F. & Frisch, M. J. Ab initio calculation of vibrational absorption and circular dichroism spectra using density functional force fields. *J. Phys. Chem.* **98**, 11623–11627 (1994).
51. Grimme, S., Antony, J., Ehrlich, S. & Krieg, H. A consistent and accurate ab initio parametrization of density functional dispersion correction (DFT-D) for the 94 elements H-Pu. *J. Chem. Phys.* **132**, 154104 (2010).

Acknowledgements We thank T. P. Russell (Materials Sciences Division, Lawrence Berkeley National Laboratory) for his support in synchrotron scattering measurements and for assistance with data analysis. Y.L., Z.-a.X., H.X. and J.W. disclose support for the research of this work from the National Natural Science Foundation of China (grant numbers T2293760 and T2293762) and the Strategic Priority Research Program of the Chinese Academy of Sciences (grant numbers XDB1030000 and XDB1270000). H.X. discloses extra support from the Key Research Program of the State Key Laboratory of Cryogenic Science and Technology (grant number 2025000402). J.L. discloses support from the National Natural Science Foundation of China (grant number 52273220). L.W., C.Z. and W.-H.F. disclose support from the National Key Research and Development Program of China (grant number 2024YFA1509600), the Beijing Natural Science Foundation (grant number JQ24005) and the Training Program of the Major Research Plan of the National Natural Science Foundation of China (grant number 92477140). G.S. and J.C. disclose support from the Science and Technology Commission of Shanghai Municipality (grant number 24010700200). J.C. discloses extra support from the Postdoctoral Fellowship Program of CPSF (grant numbers GZC20252186 and 2025M783410). X.C.Z. discloses support from the Hong Kong Global STEM Professorship Scheme and the General Research Fund of the Research Grants Council of Hong Kong (grant numbers 11204123 and 11302225). H.S., M.J., X.W., Z.S., F.B. and Z.-K.X. declare no relevant funding.

Author contributions J.W. conceived of the project. J.W. and Y.L. initialized the work. Y.L. led the experimental work, contributed to the overall conceptual framework. Y.L. and Z.-a.X. designed the experimental setups and performed data acquisition and curation. H.X. performed the experimental validation. L.W., C.Z. and X.C.Z. conducted molecular dynamics simulations, DFT calculations and theoretical analysis. All authors analysed and discussed the data. H.X., Y.L., L.W. and X.W. drafted the paper. H.S., M.J., J.L., J.C., G.S., Z.-K.X. and W.-H.F. provided suggestions to enhance the clarity of the experimental description. X.W. designed the synchrotron scattering experiments and collected the data at the Advanced Light Source. Y.L., Z.-a.X. and H.X. contributed to synchrotron data collection at the Shanghai Synchrotron Radiation Facility. X.W., H.X., Z.S. and F.B. analysed the synchrotron radiation wide-angle X-ray scattering data. All authors revised the paper.

Competing interests The authors declare no competing interests.

Additional information

Supplementary information The online version contains supplementary material available at https://doi.org/10.1038/s41586-026-10765-4.

Correspondence and requests for materials should be addressed to Han Xue, Chongqin Zhu, Xiao Cheng Zeng or Jianjun Wang.

Peer review information *Nature* thanks the anonymous reviewers for their contribution to the peer review of this work. Peer reviewer reports are available.

Reprints and permissions information is available at http://www.nature.com/reprints.

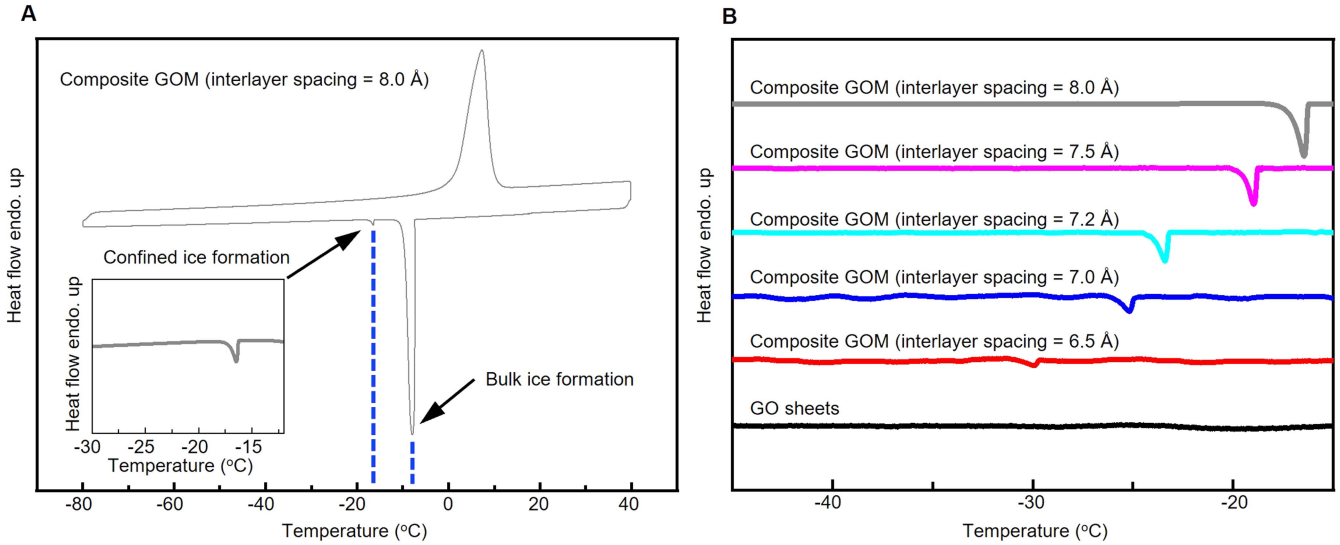

Extended Data Fig. 1 | Low-temperature DSC measurements of GO-based membranes. (**A**) DSC profiles for the cooling and warming of the GOM sample with an interlayer spacing of 8.0 Å. The inset at the bottom left highlights the enlarged peak associated with the freezing of confined water. (**B**) DSC profiles recorded during the cooling of confined water in the GOMs with varying interlayer spacings. No confined ice formation was observed in the pristine GO sheets (black line). In contrast, distinct freezing behaviors were detected in the GOMs with different interlayer spacings: red line, 6.5 Å; blue line, 7.0 Å; cyan line, 7.2 Å; magenta line, 7.5 Å; and gray line, 8.0 Å.

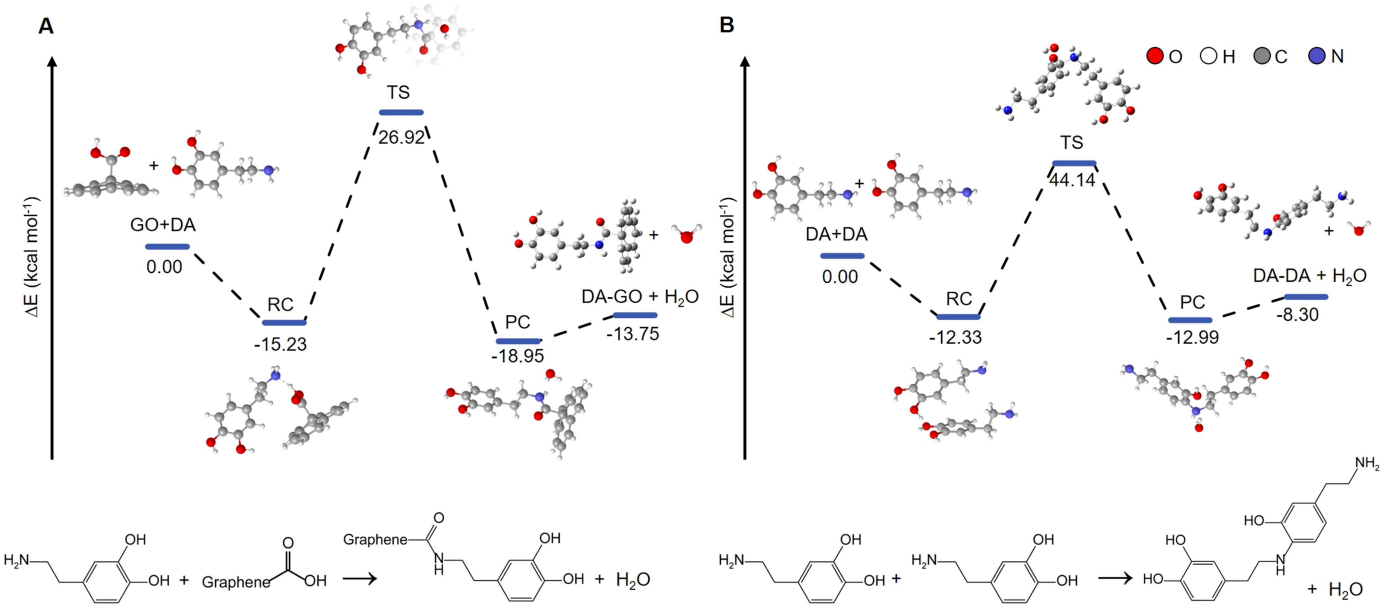

Extended Data Fig. 2 | Energy profiles for the reaction between DA molecules and functional groups on GO, and for the reaction between two DA molecules. (**A**) Energy profiles for the reaction of DA with the GO carboxyl group. (**B**) Energy profiles for the self-polymerization of DA. The relative energies (in kcal mol^{-1}) of the reactant complexes (RCs). transition states (TSs), and product complexes (PCs) calculated at the B3LYP/6-311 + + G (d, p) level of theory with Grimme's D3 dispersion corrections and the PCM solvation model (water).

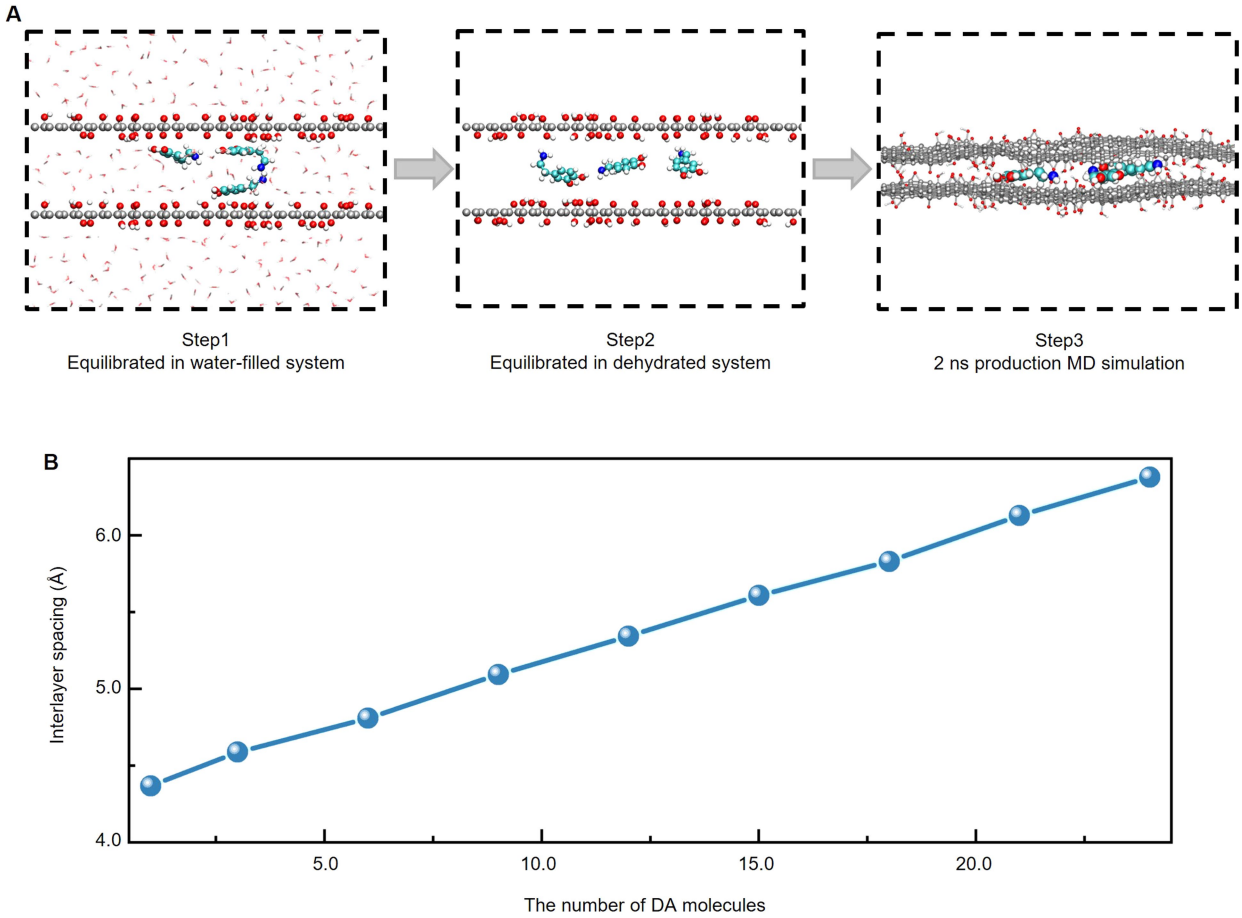

Extended Data Fig. 3 | A mechanistic description of continuous tunability for the interlayer spacings. (**A**) Schematic illustration of the simulation procedure for investigating how DA molecules in assembled pillars affect interlayer spacing. The simulation began by placing an assembled DA pillar between GO layers in aqueous solution, with all GO carbon atoms fixed, followed by MD simulations to achieve equilibrium configuration (Step 1). After reaching equilibrium, all water molecules were removed while maintaining GO carbon fixed, and additional MD simulations were performed to obtain the equilibrium state of the anhydrous system (Step 2). Finally, a 2-ns MD simulation with all atoms freely moving was conducted for analysis (Step 3). Blue spheres represent nitrogen atoms, the cyan and gray spheres represent carbon atoms in the reactive molecules and GO nanosheets, red and white spheres denote oxygen and hydrogen atoms, respectively. (**B**) The average interlayer spacing between GO sheets as a function of the number of DA molecules in assembled DA pillar. The interlayer spacing was determined by calculating the average z-coordinate difference between opposing GO sheets, with error bars indicating the standard deviations of temporal fluctuations (shown by light blue shading).

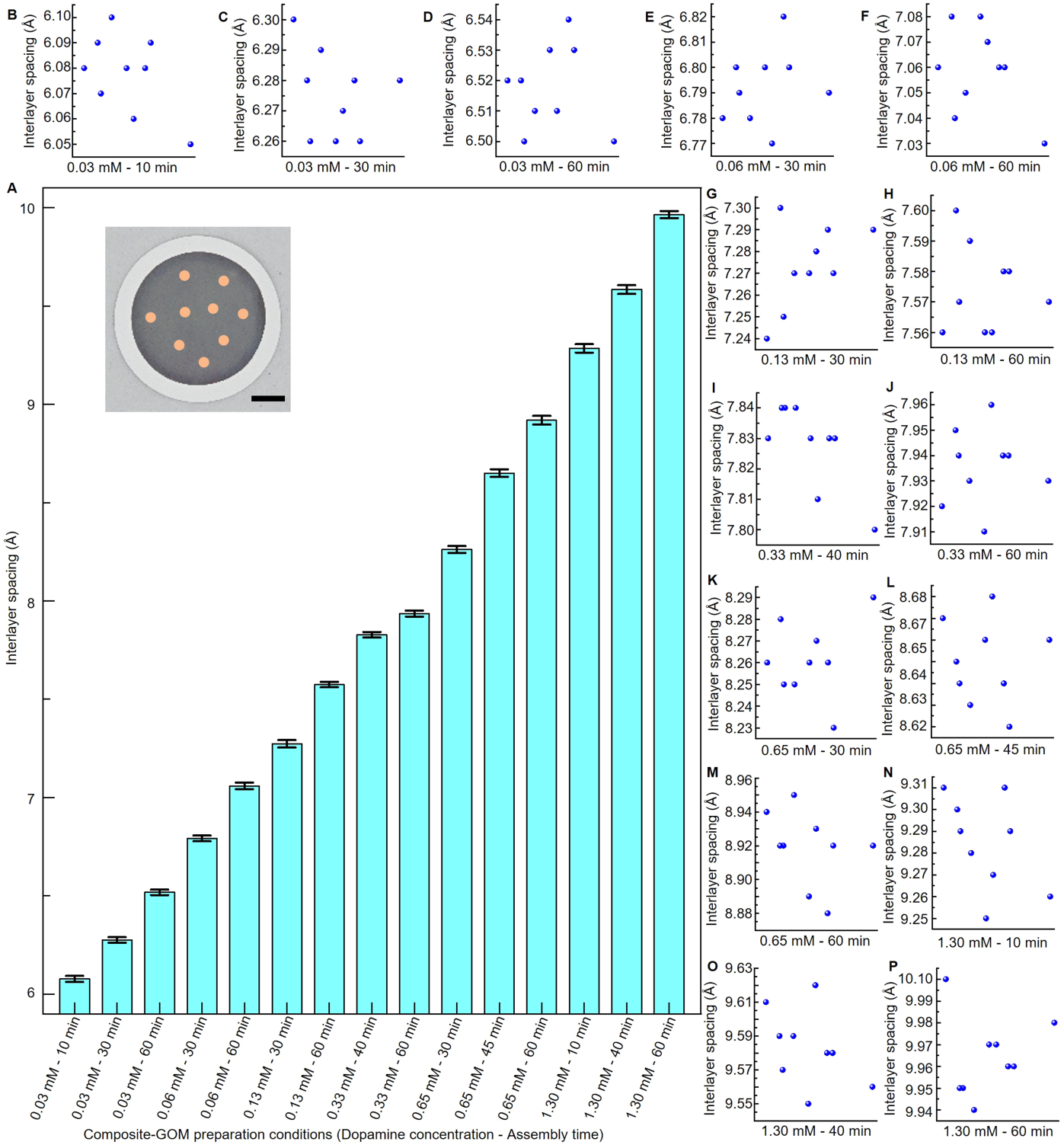

Extended Data Fig. 4 | Uniformity of fabricated composite GOMs. (**A**) Uniformity is defined as the standard deviation of XRD-measured interlayer spacings acquired from 9 distinct positions on the same single membrane. The uniformity of interlayer spacing of composite GOMs is examined under varied fabrication conditions. The error bars are the standard deviations. The inset in the upper left shows an optical image of one selected composite GOM. Scale bar, 1 cm. (**B-P**) Scatter plots of the uniformity of interlayer spacing under different fabrication conditions, where nine independent XRD measurements on one membrane sample were recorded for each fabrication condition.

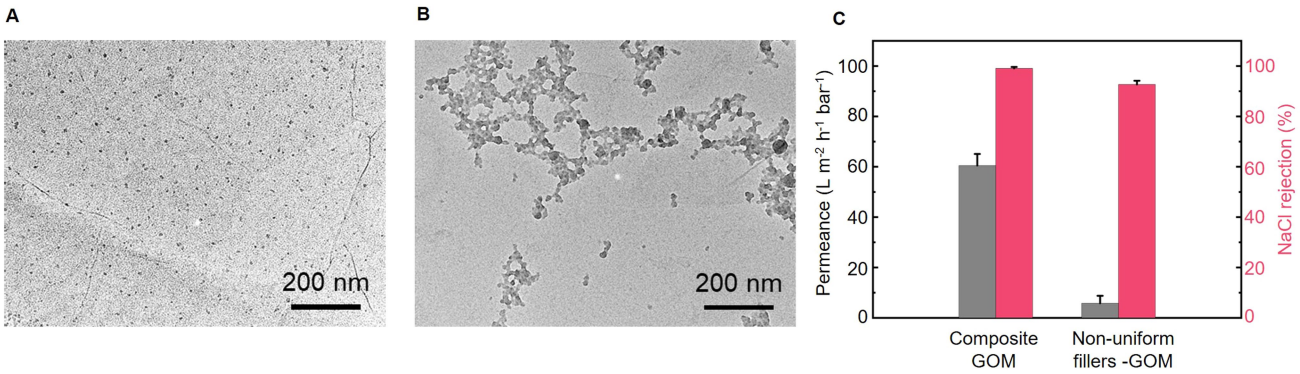

Extended Data Fig. 5 | Effect of DA assembly on nanopillar uniformity and water permeance through the GOMs. TEM images of the GOM after treatment with 0.06 mM DA solution via two different approaches: (**A**) assembly-reaction method under confinement, and (**B**) the traditional covalent strategy without prior assembly. As shown in (**B**), the DA distribution is non-uniform using the conventional strategy. (**C**) The presence of non-uniform fillers within the GOM can partially obstruct the water transport channels, consequently diminishing the overall water permeate. The error bars indicate the standard deviation; each average value is calculated from more than 5 measurements. As shown in Extended Data Fig. 5a, the increased size of DA assembly indicates that DA molecules tend to accumulate and assemble rather than distributing randomly throughout the interlayer space. This observation supports a mechanism in which nanoconfined water drives molecular localization and aggregation, minimizing undesired reactions in the carbon-carbon interlayer regions in the later reaction process. For the DA molecules, we further illustrate that random reactions throughout the interlayer without the assembly process could lead to the formation of larger fillers with uncontrolled size as shown in Extended Data Fig. 5b. Moreover, this irregularly distributed matter can disrupt the interlayer space including carbon-carbon regions and reduce water permeation due to obstruction of high-flux transport pathways (Extended Data Fig. 5c). Therefore, the observed spatial selectivity of the DA assembly is a key principle underpinning the high performance of the membrane.

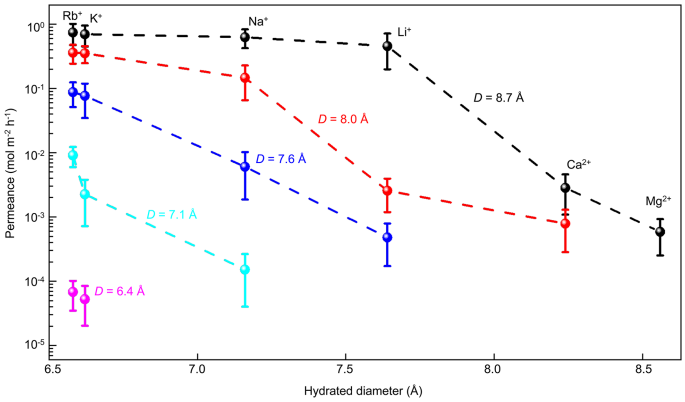

Extended Data Fig. 6 | Metal ion permeation rates of Rb^+, K^+, Na^+, Li^+, Ca^{2+}, and Mg^{2+} through the GOMs with different wet-state interlayer spacings. Experiments were performed at 25 °C under continuous cross-flow at 8 bar using membranes with an effective area of 10.6 cm^2. A 0.05 M aqueous solution of each salt was used as feed. After discarding the initial 10 mL of permeate, samples were collected over 2 h. Each data point represents the mean of 10 independent measurements, with error bars indicating the standard deviation. The results reveal a sharp cutoff in salt permeation when the interlayer spacing is adjusted to match the hydration diameter of the ions, indicating that the interlayer spacing control enables composite GOMs to function as highly selective ion filters.

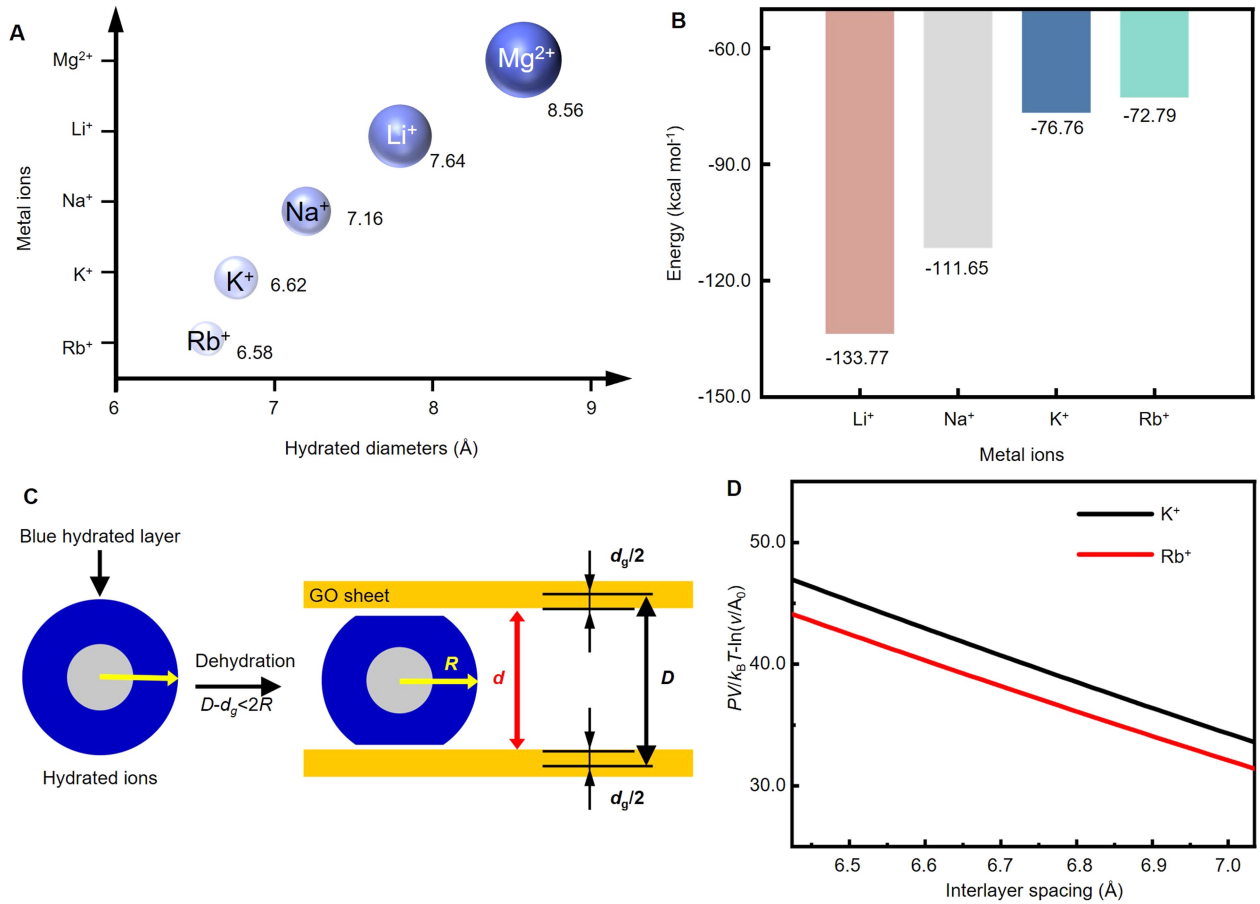

Extended Data Fig. 7 | Hydrated ionic sizes, hydration energies, and dehydration energies for selected metal ions. (**A**) A reference for the hydrated ionic sizes of rubidium (Rb^+), potassium (K^+), sodium (Na^+), lithium (Li^+), and magnesium (Mg^{2+}). The largest dark blue sphere represents the size of magnesium ions, the second largest blue sphere represents the size of lithium ions, the third largest medium blue sphere represents the size of sodium ions, the fourth largest light-blue sphere represents the size of potassium ions, and the smallest light-cyan sphere represents the size of rubidium ions. (**B**) Hydration energies of ion-water clusters (ion-$(H_2O)_6$) for Rb^+, K^+, Na^+, Li^+. Cluster structures were optimized using Gaussian 09 software program at the DFT B3LYP level with a mixed basis set: the SDD pseudopotential for the cation and the 6-311 + + G (d, p) basis set for water molecules, where the (d, p) notation indicates the addition of polarization functions (d-type on heavy atoms and p-type on hydrogen atoms). (**C**) Schematic illustration of the partial dehydration process, where the gray spheres represent ions, the blue regions denote the hydration shells, and the orange plates correspond to GO sheets. (**D**) Dehydration energy (ΔE) for different ions (Rb^+ – red line, K^+ – black line) entering the interlayer channels of the GOMs with varying interlayer spacings. The energy values were computed using Eqs. (1) - (6). In the GOMs, the free channel height is given by $d = D - d_g$, where D is the interlayer spacing and d_g is the graphene thickness (3.4 Å). For a single sub-nanochannel, ion transport takes place only when $\boldsymbol{d}$ exceeds the vertical dimension of the partially dehydrated ions (Extended Data Fig. 7c). This implies that the confined environment inside the sub-nanochannel promotes partial dehydration of the hydrated ions. The number of water molecules removed during this process can be estimated as follows: $\Delta N = \frac{N_h}{V_h} V_{de}$ (1) where ΔN, N_h, V_h, and V_{de} denote the dehydration water number, hydration number, hydration volume and dehydration volume, respectively, as shown in Extended Data Fig. 7c. Accordingly, the dehydration energy can be calculated using the following equation: $\Delta E = \Delta N \frac{|E_h|}{N_h}$ (2) where ΔE, and E_h represent the dehydration energy required for an ion to enter a sub-nanochannel, and the hydration energy of the ion in bulk water, respectively. The dehydration volume (V_{de}) and hydration volume (V_h) can be derived from the spherical and spherical cap volume, respectively: $V_{de} = \frac{2}{3}\pi\left(R - \frac{d}{2}\right)^2\left(2R + \frac{d}{2}\right)$ (3) $V_h = \frac{4}{3}\pi R^3$ (4) where R is the radius of the hydrated ion. It is evident that ion transport, similar to typical chemical reactions, is an activated process. Consequently, its behaviour should adhere to the Arrhenius equation, a conclusion that is supported by previous research: $\upsilon = A_0 e^{-\frac{E_a}{k_B T}}$ (5) where $\boldsymbol{\upsilon}$ represents the ion flow rate, T is the temperature, k_B is the Boltzmann constant, A_0 is the pre-factor corresponding to the attempt frequency, and E_a is the activation energy. The activation energy can be roughly divided into two components: $E_a = \Delta E - PV$ (6) where P is pressure, and V represents the effective volume of an ion in a sub-nanochannel.

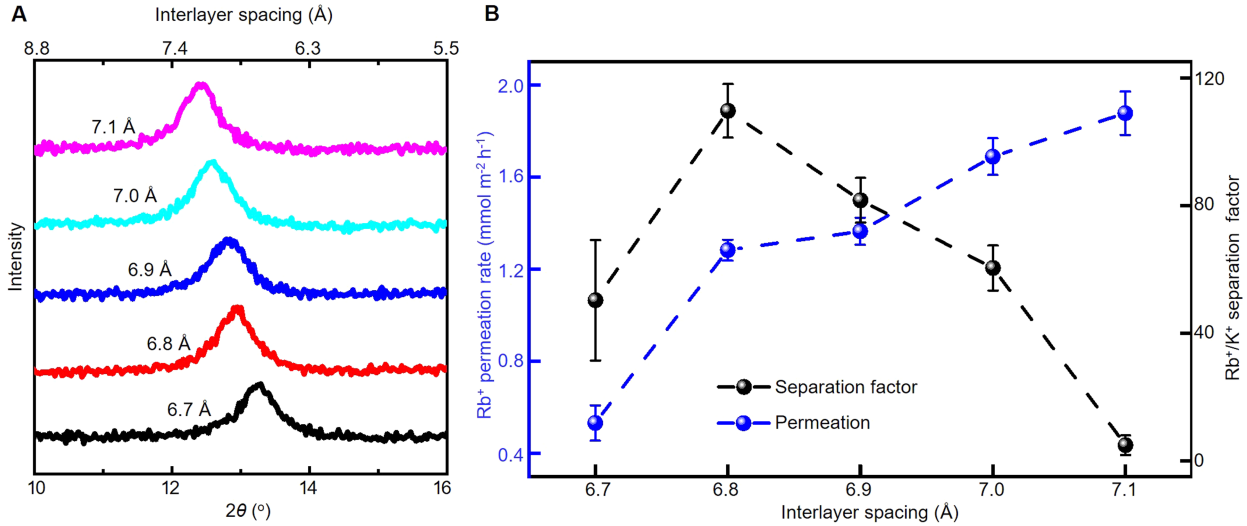

Extended Data Fig. 8 | Effect of interlayer spacing on Rb^+/K^+ separation factor and Rb^+ permeation. Dependence of the Rb^+/K^+ separation factor on interlayer spacings of 6.7 Å (black line and sphere), 6.8 Å (red line and sphere), 6.9 Å (blue line and sphere), 7.0 Å (cyan line and sphere), and 7.1 Å (magenta line and sphere). (**A**) XRD patterns of membranes with different interlayer spacings, confirming the precise control of the interlayer distance. (**B**) Relationship between the Rb^+ ion permeation (the blue points and line) and the Rb^+/K^+ ion separation factor (the black points and line) for membranes with different interlayer spacings. The permeance and separation-factor values were each averaged from five independent experiments. Error bars indicate the standard deviations. In this experiment, a feed solution consisting of a 1:1 mixture of 0.5 mM RbCl and 0.5 mM KCl was used. The filtration was conducted with effective membrane area of 10.6 cm^2 and the operation pressure of 5 bar. The ion concentration was measured with 4 h after the permeability test.

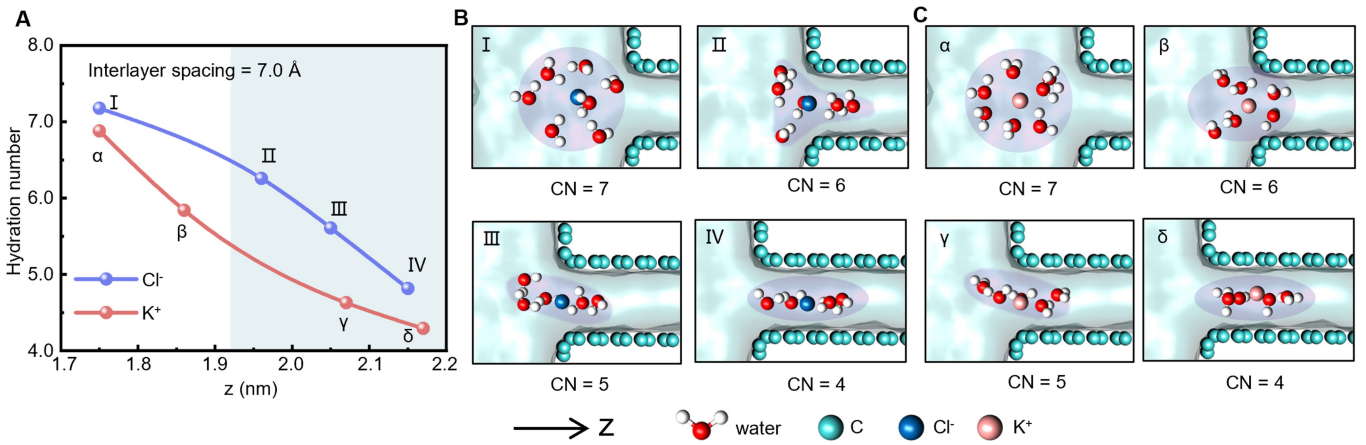

Extended Data Fig. 9 | The partial dehydration process of ions upon entering graphene nanochannels. (**A**) Hydration coordination number of a Cl^- ion and a K^+ ion as it moves from bulk solution into a graphene channel with an interlayer spacing of 7.0 Å. The z-axis is parallel to the sub-nanochannel, and the light-gray shadow area marks the position of the interlayer sub-nanochannel ($z > 1.92$ nm). I (α), II (β), III (γ), and IV (δ) denote the order of the snapshots presented in (**B**) and (**C**), corresponding to the states before entering the channel, at the channel entrance, just inside the channel, and stabilized within the channel, respectively. The inset provides a schematic illustration of the simulation system. (**B-C**) Snapshots of hydration structures corresponding to different positions in (**A**). Cyan spheres represent graphene carbon atoms, blue spheres represent Cl^- ions, pink spheres represent K^+ ions, red and white spheres denote oxygen and hydrogen atoms of coordinating water molecules, respectively, with light-purple shading around the ion highlighting the first solvation shell. Remaining water molecules are shown as a light-blue shading.

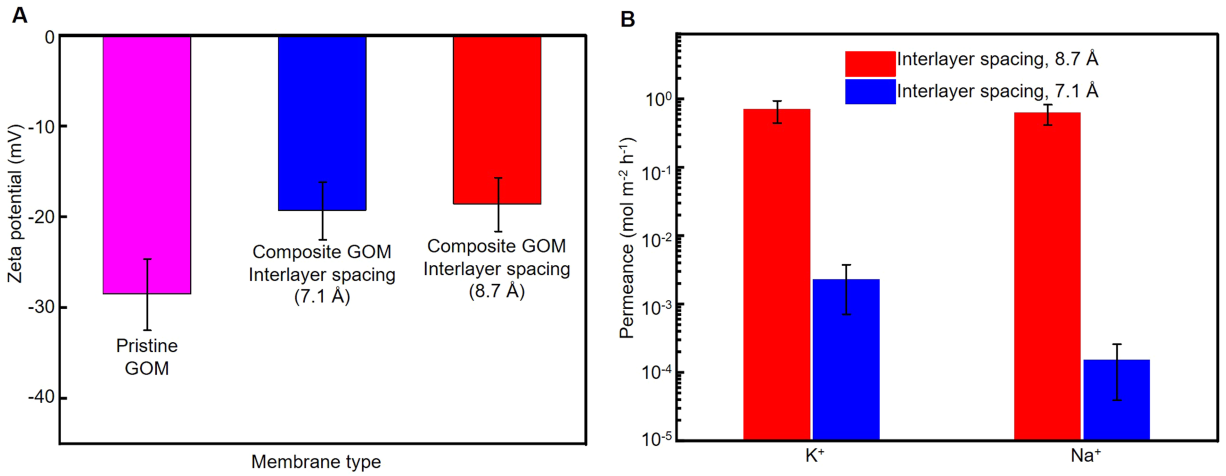

Extended Data Fig. 10 | Surface properties and ion permeability of fabricated composite GOMs with different interlayer spacings. (**A**) Evaluation of GO-based membrane surface charge by zeta potential, obtained using a SurPASS electrokinetic analyzer through streaming potential measurements. 1 mM KCl solution was used to measure the zeta potential of the membrane initially under neutral pH. Each data point was averaged over 5 independent experiments. Error bars are the standard deviation. The magenta bar denotes the pristine GOM, whereas blue and red bars represent the GOMs with interlayer spacings of 7.1 Å and 8.7 Å, respectively. (**B**) Permeance of K^+ and Na^+ ions through the GOMs with interlayer spacings of 7.1 Å (blue) and 8.7 Å (red). The permeance of different ions through the GOMs varies depending on the interlayer spacing. The data for permeance were averaged over 10 independent experiments. Error bars indicate the S.D.